NANO · MICRO small
www.small-journal.com

Zn^{2+} Pre-Intercalation Stabilizes the Tunnel Structure of MnO_2 Nanowires and Enables Zinc-Ion Hybrid Supercapacitor of Battery-Level Energy Density

Qiang Chen, Jialun Jin, Zongkui Kou, Cong Liao, Ziang Liu, Liang Zhou, John Wang,* and Liqiang Mai*

Although there has been tremendous progress in exploring new configurations of zinc-ion hybrid supercapacitors (Zn-HSCs) recently, the much lower energy density, especially the much lower areal energy density compared with that of the rechargeable battery, is still the bottleneck, which is impeding their wide applications in wearable devices. Herein, the pre-intercalation of Zn^{2+} which gives rise to a highly stable tunnel structure of Zn_xMnO_2 in nanowire form that are grown on flexible carbon cloth with a disruptively large mass loading of 12 mg cm^{-2} is reported. More interestingly, the Zn_xMnO_2 nanowires of tunnel structure enable an ultrahigh areal energy density and power density, when they are employed as the cathode in Zn-HSCs. The achieved areal capacitance of up to 1745.8 mF cm^{-2} at 2 mA cm^{-2}, and the remarkable areal energy density of 969.9 µWh cm^{-2} are comparable favorably with those of Zn-ion batteries. When integrated into a quasi-solid-state device, they also endow outstanding mechanical flexibility. The truly battery-level Zn-HSCs are timely in filling up of the battery-supercapacitor gap, and promise applications in the new generation flexible and wearable devices.

1. Introduction

With the rapid development of wearable and portable electronics, there is a systematic demand for a full range of energy storage devices, with high areal energy and power density, fast charge/discharge rate, long cycling lifetime, and mechanical flexibility, which are being extensively explored.[1] In this regard, on the one hand, supercapacitors satisfy those high power, fast charge/discharge, and long cycling requirements.[2] On the other hand, rechargeable batteries offer relatively high energy density, due to abundant redox reactions of the active materials, while they suffer from the short cycling lifetime and low power density.[3] Therefore, the hybrid supercapacitors (HSCs), where capacitor-type electrode acts as the anode and battery-type electrode acts as the cathode can bridge the large gap between supercapacitors and batteries, by integrating the advantages of both, on the key parameters such as energy and power density.[4] The traditional alkaline hybrid supercapacitors provide a high energy density, relied on the redox reaction of the battery-like electrode, but with the trade-off in low power density and short cycling lifetime.[5] This is due to the poor electronic conductivity of the battery-type electrodes, which limits the rate capability for high power performance.[6] The overall performance reported for hybrid supercapacitors, in both energy density and power density, is far behind those of rechargeable batteries. Therefore, a truly battery-level HSC would represent a major technical breakthrough.

Indeed, HSCs based on alkaline metal ions, such as Li^+,[7] Na^+,[8] and K^+[9] have been investigated widely, and enormous progress has been made in recent years. Although some of them have demonstrated a high energy density, while preserving the high power density of supercapacitors (SCs), there are still numerous problems in terms of overall performance. For example, use of any organic electrolytes and excessive active reactions of those alkalis can present serious safety risks. For some of these alkaline metals, there can also be a poor long-term sustainability issue, similar issue as for the lithium batteries. In contrast, the energy storage devices making use of multivalent cations (Zn^{2+},[10] Ca^{2+},[11] Al^{3+},[12] etc.) can deliver high and unique performance, where Zn^{2+} is one of the best known examples. Indeed, among these multivalent cations, zinc-ion HSCs have attracted a considerable amount of attention, thanks to its low cost, abundant sources, high safety, and environmental friendly features,[13] making it one of the most promising candidates for the new generation energy storages. Zhang et al. assembled flexible Zn-HSCs where reduced graphene oxide/carbon nanotube (rGO/CNT) fiber and Zn/C fiber act as cathode and anode, respectively, indicating the well application of Zn-HSCs in wearable electronics.[14] By far, there

Q. Chen, J. Jin, C. Liao, Z. Liu, Prof. L. Zhou, Prof. L. Mai
State Key Laboratory of Advanced Technology
for Materials Synthesis and Processing
Wuhan University of Technology
Wuhan 430070, China
E-mail: liangzhou@whut.edu.cn
Q. Chen, Dr. Z. Kou, Prof. J. Wang
Department of Materials Science and Engineering
National University of Singapore
Singapore 117574, Singapore
E-mail: msewangj@nus.edu.sg
The ORCID identification number(s) for the author(s) of this article can be found under https://doi.org/10.1002/smll.202000091.

DOI: 10.1002/smll.202000091

are several studies on Zn-HSCs, where both electrodeposited Zn nanosheets and Zn foil have been used as the anode.[4c,d,15] However, it is still very challenging to control the fading of Zn nanosheets and formation of zinc dendrites in Zn foil, which is known to affect efficiency of the stripping/plating processes in the anode, during charge/discharge processes, and adversely impact the electrochemical performance. In this connection, Ma et al. assembled a different configuration of the γ-MnO_2// AC Zn-HSCs.[16] However, in the Zn^{2+} charging and discharging processes, the structure of MnO_2-based materials is unstable.[17] Liu et al. have reported that the structural stability can be improved by pre-intercalated K^+ into the tunnel structure α-MnO_2.[18] Although the cycling performance was improved to a certain degree, the structure still undergoes an unstable transformation (i.e., transformation into layered structure δ-MnO_2), when further intercalated in Zn^{2+}. Therefore, structural stability is one of the key factors in the design of Zn-HSCs electrode materials.

Herein, in contrast, we report a highly stable tunnel structure of Zn_xMnO_2 in nanowires grown on mechanically flexible carbon cloth, which are successfully made by pre-intercalation of Zn^{2+} and with a disruptively large mass loading of 12 mg cm^{-2}. The Zn^{2+} stabilized tunnel structure of Zn_xMnO_2 at ultrahigh mass loading grown on flexible carbon cloth is developed by one-step hydrothermal process, where the pre-intercalation of Zn^{2+} transforms the layered δ-MnO_2 nanosheets into tunnel-structured Zn_xMnO_2 nanowires of high stability. In Zn-HSCs, the insertion/extraction on the Zn_xMnO_2 nanowires cathode and the adsorption/desorption on the activated carbon cloth (ACC) anode enable an outstanding electrochemical performance. The as-prepared Zn-HSCs present an ultrahigh areal capacitance of 1745.8 mF cm^{-2} at 2 mA cm^{-2} with a wide operating voltage window of 0–2 V. They also deliver a remarkable areal energy density of 969.9 μWh cm^{-2} and a peak areal power density of 20.1 mW cm^{-2}. The rechargeable Zn-HSCs show a superior capacity retention of 83.1% after 5000 cycles. In addition, when constructed into a quasi-solid-state device, they endow an outstanding capacitance of 1446.6 mF cm^{-2}, and the maximum areal energy density and peak power density of 803.6 μWh cm^{-2} and 10.0 mW cm^{-2}, respectively. They make Zn-HSCs truly reach up to battery-level, and also with the desired mechanical flexibility and long-term cycling ability.

2. Results and Discussion

The synthesis processes of Zn_xMnO_2 nanowires and MnO_2 nanosheets are schematically illustrated in **Figure 1**. The tunnel-type zinc-ion stabilized α-MnO_2 (Zn_xMnO_2) nanowires were synthesized via a simple one-step hydrothermal method. Interestingly, when the zinc source was not added to the precursor solution, the layered structure δ-MnO_2 (MnO_2) nanosheets was obtained.

To confirm the phase information, we scrupulously study the X-ray diffraction (XRD) patterns (**Figure 2**a) and the Raman spectra (Figure S1, Supporting Information). The XRD pattern of Zn_xMnO_2 nanowires shows seven main characteristic peaks at 12.8°, 18.1°, 28.8°, 37.5°, 41.9°, 49.8°, and 60.3°, indexing to (110), (200), (310), (211), (301), (411), and (521) planes of the α-MnO_2 (JCPDS No. 44-0141),[19] respectively. Comparatively, the XRD pattern of MnO_2 nanosheets displays main four peaks at 12.6°, 25.3°, 36.9°, and 65.6°, corresponding to the (001), (002), (11-1), and (31-2) planes of δ-MnO_2 (JCPDS No. 42-1317).[20] The Raman band at 644 cm^{-1} stands for the α-MnO_2 while the Raman band at 631 cm^{-1} stands for the δ-MnO_2,[21] which are in good agreement with XRD results. The scanning electron microscope (SEM) images in Figure 2b,c and Figure S2 (Supporting Information) exhibit the Zn_xMnO_2 nanowires and MnO_2 nanosheets are uniformly covered on the surfaces of the CC, respectively. Impressively, the mass loading of the Zn_xMnO_2 nanowires on the CC is measured to be 12 mg cm^{-2}, which is the highest level among reported electrode materials applied in both supercapacitors and batteries (Table S1, Supporting Information). Such a high mass loading provides a great promise for enhancing the overall areal energy density of HSCs. As shown in Figure 2d, Zn_xMnO_2 nanowires on the CC present a thickness of up to 4.2 μm. The morphological feature of the Zn_xMnO_2 nanowires is further investigated by the transmission electron microscopy image (TEM, Figure 2e), in which the length of nanowire is about 1.1 μm. In addition, the selected area electron diffraction image (SAED, the inset in Figure 2e) further confirms its single crystalline nature. The high-resolution TEM (HRTEM) image of the Zn_xMnO_2 nanowires is depicted in Figure 2f, where two lattice fringes of 0.69 and 0.31 nm can be indexed to (110) and (310) planes of α-MnO_2. In order to reveal the elements distribution along a single nanowire, the element mapping of zinc, manganese, and oxygen elements are displayed in Figure 2g, in which the uniform coverage of zinc can be clearly seen. For comparison, the TEM, HRTEM, and element mapping of MnO_2 counterpart are also provided in Figure S3 (Supporting Information), and the energy-dispersed spectra (EDS) of Zn_xMnO_2 and MnO_2 are compared in Figure S4 (Supporting Information).

Moreover, the X-ray photoelectron spectroscopy (XPS) survey spectra were performed to identify and compare the chemical states of each elements on the surfaces of Zn_xMnO_2 and MnO_2. The Mn, O, and C elements are detected in both the samples while the Zn only detected in the Zn_xMnO_2 nanowires (Figure S5, Supporting Information). The Zn 2p spectra (Figure 2h) display the characteristic peaks at binding energies of 1044.6 and 1021.5 can be assigned to Zn^{2+} $2p_{1/2}$ and Zn^{2+} $2p_{3/2}$, revealing the dominant valence state of Zn^{2+} in the Zn_xMnO_2. As displayed in Figure 2i, the Mn 2p spectra show two peaks at 641.8 and 653.5 eV in both MnO_2 and Zn_xMnO_2 sample, corresponding to $2p_{3/2}$ and $2p_{1/2}$ signals of Mn (IV). Notably, in comparison to MnO_2, the Zn_xMnO_2 nanowires exhibit two additional peaks in Figure 2i that emerged at binding energies of 641.3 and 652.4 eV, which are the typical line positions for Mn $2p_{3/2}$ and Mn $2p_{1/2}$ signals of Mn^{3+}, respectively.[22] Considering the results mentioned above, we can determine the coordination structure of Mn in the Zn_xMnO_2 nanowires after Zn intercalation, which is beneficial for promoting the stability of the tunnel-type Zn_xMnO_2 and the electrochemical performance.

Before assembling the Zn-HSCs, we performed oxygen annealing process to activate the CC (The detailed characterization can be seen in Figures S6 and S7, Supporting Information), which will act as the anode of Zn-HSCs. **Figure 3**a exhibits the cyclic voltammetry (CV) curves of individual Zn_xMnO_2 cathode

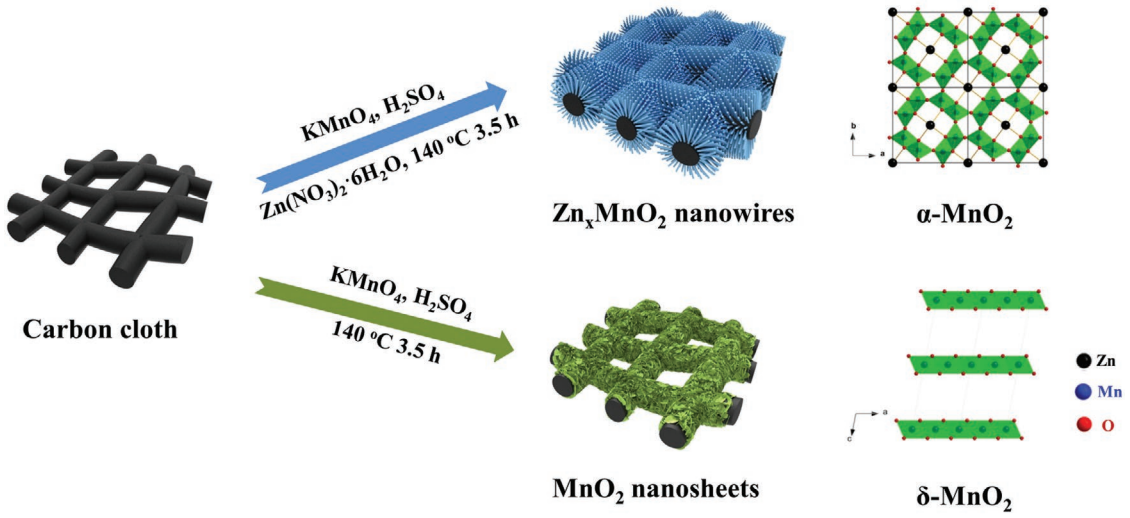

Figure 1. Schematic diagram illustrating different reaction processes of MnO_2 nanosheets and Zn_xMnO_2 nanowires.

and ACC anode, presenting the adsorption/desorption in ACC anode and the insertion/extraction in Zn_xMnO_2 cathode. Two redox peaks can be seen at 0.33/0.88 V (vs saturated calomel electrode) of the CV curve of Zn_xMnO_2. Besides, wonderful rectangular CV and galvanostatic charge/discharge (GCD) curves (Figure S8, Supporting Information) of ACC anode and GCD

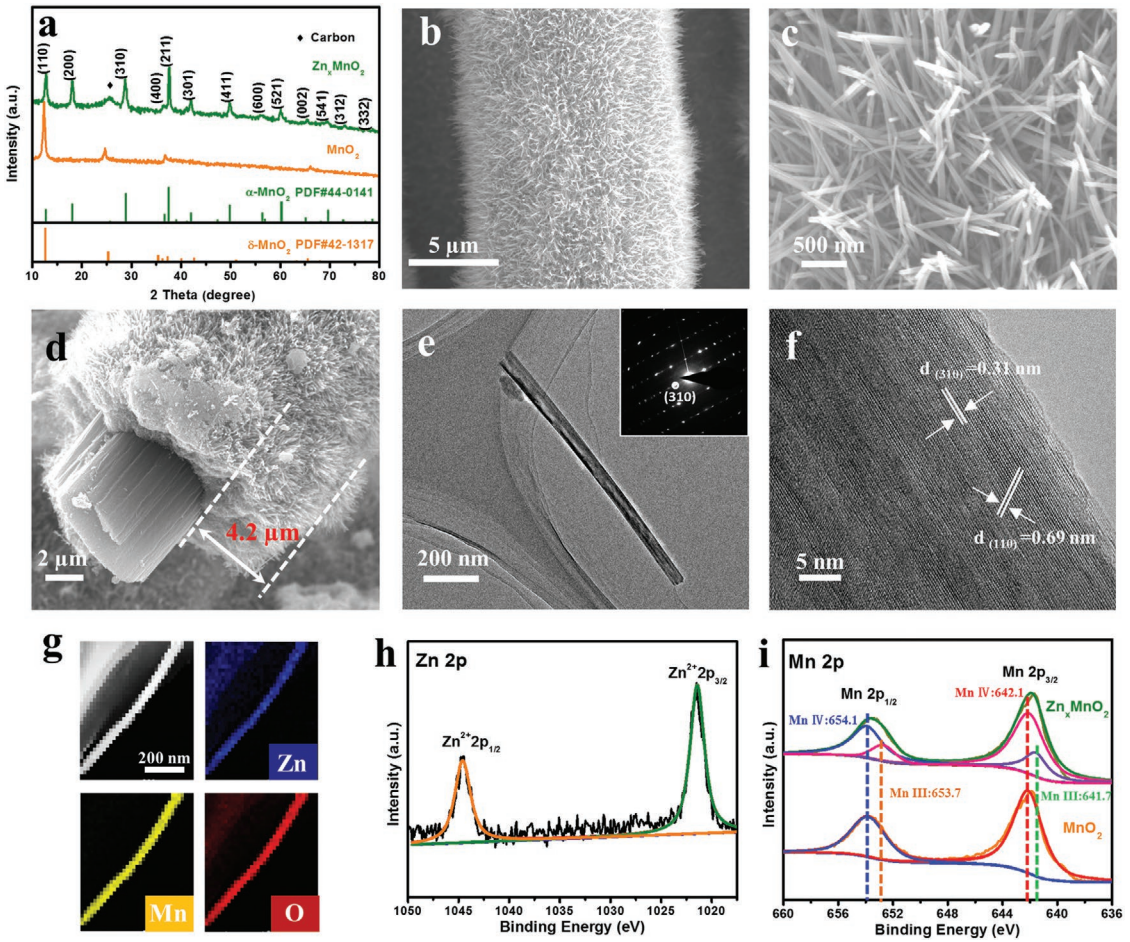

Figure 2. a) XRD patterns of the MnO_2 and Zn_xMnO_2. b,c) SEM images and d) sectional view of the Zn_xMnO_2 nanowires. e) TEM, SAED (the inset), and f) HRTEM. g) Element mapping of the Zn_xMnO_2. h) Core-level Zn 2p XPS spectra of the Zn_xMnO_2. i) Core-level Mn 2p XPS spectra of the MnO_2 and Zn_xMnO_2.

curves (Figure S9, Supporting Information) with clear charge/discharge platform of the Zn_xMnO_2 nanowires are obtained in three-electrode system, which shows the splendid capacitor and typical battery performance of the ACC anode and the Zn_xMnO_2 cathode in the Zn-HSCs, respectively. To further assess the actual properties of Zn_xMnO_2 nanowire cathode, we employed the ACC as the anode and assembled the Zn_xMnO_2//ACC Zn-HSCs in an aqueous electrolyte (2 M $ZnSO_4$ and 0.4 M $MnSO_4$) with a comparison of the MnO_2//ACC Zn-HSCs. As shown in Figure 3b, the CV curves of these two Zn-HSCs have no obvious battery behaviors, which can also be verified in GCD curves (Figure 3c), indicating that the main characteristic of the Zn-HSCs is still capacitive behavior. The CV curves of these two Zn-HSCs at various scan rates from 1 to 40 mV s^{-1} are displayed in Figure 3d and Figure S10a (Supporting Information), clearly indicating a higher specific capacitance of Zn_xMnO_2//ACC Zn-HSCs than MnO_2//ACC Zn-HSCs. Moreover, the electrochemical performance of these two Zn-HSCs is also investigated by GCD at different current density between 2 and 20 mA cm^{-2} (Figure 3e and Figure S10b, Supporting Information). According to the GCD curves, the Zn-HSCs show a wider voltage window than the other Zn-HSCs and HSCs.[4c,d,15,23] Figure 3f exhibits the functions of the areal capacitance of Zn_xMnO_2//ACC and MnO_2//ACC Zn-HSCs collected at various current density and the peak areal capacitance of the Zn_xMnO_2//ACC Zn-HSCs reaches 1745.8 mF cm^{-2} (gravimetric specific capacity ≈ 145.5 F g^{-1}) at 2 mA cm^{-2}, which is superior to most supercapacitors (Table S2, Supporting Information), such as AC//Zn Zn-HSC,[24] CoHCF//AC HSC,[25] and $Ni_{0.25}Mn_{0.75}O$@C// AC Li-ion HSCs.[26] As depicted in Figure 3g, the GCD curves of the Zn_xMnO_2//ACC Zn-HSCs are collected at 6 mA cm^{-2} with an operational voltage window ranging from 0.6 to 2.0 V, demonstrating the voltage of as-assembled Zn-HSCs can be stabilized up to 2.0 V. Figure 3h presents the electrochemical impedance spectroscopy (EIS) of the Zn_xMnO_2//ACC and MnO_2//ACC Zn-HSCs where the semicircles represent charge transfer resistance (R_{ct}) and the slopes are related to Zn^{2+} diffusion resistance in the electrode materials. The Zn_xMnO_2//ACC Zn-HSCs show smaller R_{ct} (35.96 vs 62.09 Ω) and faster diffusion velocity than those of MnO_2//ACC Zn-HSCs.

As an exploration, we studied the effect of different electrolytes on the electrochemical performance of as-prepared Zn_xMnO_2 nanowire (Figure S11, Supporting Information). It can be found that the HSC displays a higher capacitance only in zinc-containing electrolyte, and the accession of manganese vastly improves the capacitance. To optimize the Zn^{2+} pre-intercalation amount, the feeding amount of $Zn(NO_3)_2$ was varied from 0 to 10 mmol. Both the crystalline phase and morphology of the obtained Zn_xMnO_2 are highly dependent on the $Zn(NO_3)_2$ feeding amount. With the increase of $Zn(NO_3)_2$ feeding amount, the Zn_xMnO_2 experiences a phase transformation from layered structure to tunnel structure and its morphology changes from nanosheets to nanowires. With a relatively low $Zn(NO_3)_2$ amount (≤2 mmol), the Zn_xMnO_2 shows a layered structure similar to δ-MnO_2 (Figure S12, Supporting Information) and a nanosheet morphology (Figure S13, Supporting Information). With a moderate $Zn(NO_3)_2$ feeding amount (4–6 mmol), a mixture of δ-MnO_2 phase and α-MnO_2 phase Zn_xMnO_2 is obtained. Further increase of the $Zn(NO_3)_2$ feeding amount leads to α-MnO_2 phase Zn_xMnO_2 with a tunnel structure and well-defined nanowire morphology. When coupled with ACC anode for Zn-HSCs, the Zn_xMnO_2 with a $Zn(NO_3)_2$ feeding amount of 8 mmol demonstrates the highest capacitance (Figure S14, Supporting Information). Therefore, we believe 8 mmol is the optimized $Zn(NO_3)_2$ feeding amount.

Typically, the Zn_xMnO_2//ACC Zn-HSCs reaches a remarkable cycling performance with 83.1% retention of the initial capacity after 5000 cycles at 15 mA cm^{-2} (Figure 3i) while the MnO_2//ACC Zn-HSC only affords a capacitance retention of 45.3% after 5000 cycles at the same current density. Moreover, the phase and morphology of the electrode materials remain the same after the cycling (Figures S15–S17, Supporting Information). Combining with the electrochemical performance of the Zn_xMnO_2//ACC and MnO_2//ACC Zn-HSCs, it is confirmed again that the designed tunnel-type α-Zn_xMnO_2 nanostructure is considered as the optimal MnO_2 battery-type electrode materials for Zn-HSCs.

In order to investigate the practical utilities and flexible characteristic of the promising Zn_xMnO_2 nanowires cathode and the as-assembled Zn-HSCs, the flexible quasi-solid-state Zn_xMnO_2//ACC Zn-HSCs device is assembled and the structure is schematically illustrated in **Figure 4**a. Briefly, a piece of filter paper and a polyvinyl alcohol (PVA) gel are serving as a separator and electrolyte, respectively, which sandwiched by the Zn_xMnO_2 nanowire cathode and the ACC anode.[27] The CV curves of the Zn-HSC device at scan rates ranging from 1 to 40 mV s^{-1} are shown in Figure 4b, and the GCD curves (Figure 4c) display a great capacity compared to the aqueous Zn-HSCs (73.2%), which reaches a prominent capacitance of 1446.6 mF cm^{-2} at 1 mA cm^{-2}. From Figure 4d, when the quasi-solid-state Zn-HSCs are bended to various conditions, the capacity and discharging curve keep nearly the same, indicating its excellent suitability to shape deformation. Additionally, Figure 4e further presents the areal power and energy densities of the Zn_xMnO_2//ACC Zn-HSCs device with both aqueous and quasi-solid-state electrolytes, from which the Zn_xMnO_2//ACC Zn-HSCs device can afford maximum areal energy density of 969.9 μWh cm^{-2}, peak areal power density of 20.1 mW cm^{-2} in aqueous system and the maximum areal energy density of 803.6 μWh cm^{-2}, peak areal power density of 10.0 mW cm^{-2} in quasi-solid-state system. Importantly, the areal performance of the as-prepared Zn-HSCs are considerably higher than those of many reported aqueous and quasi-solid-state energy storage devices and even comparable or higher than many Zn-ion batteries as shown in Table S2 (Supporting Information), such as $V_2O_5 \cdot nH_2O$//graphene,[28] $NaV_3O_8 \cdot 1.5H_2O$//Zn,[29] $ZnMn_2O_4$//Zn,[30] ZnHCF@MnO_2//Zn,[31] and $Zn_2V_2O_7$//Zn.[32] Impressively, as shown in the inset of Figure 4e, the thickness of the device is measured to be 0.86 mm. For a simple demonstration, we lighted up two neon signs (consisting of 14 and 52 LEDs, respectively) by connecting two devices in series. As exhibited in Figure 4f and Movies S1 and S2 (Supporting Information), the tandem devices brightened the neon signs with dazzling shine for 15 and 10 min, respectively.[33] To sum up, the outcomes mentioned above definitely suggest the ultrahigh areal energy density, flexibility, and practical application of the

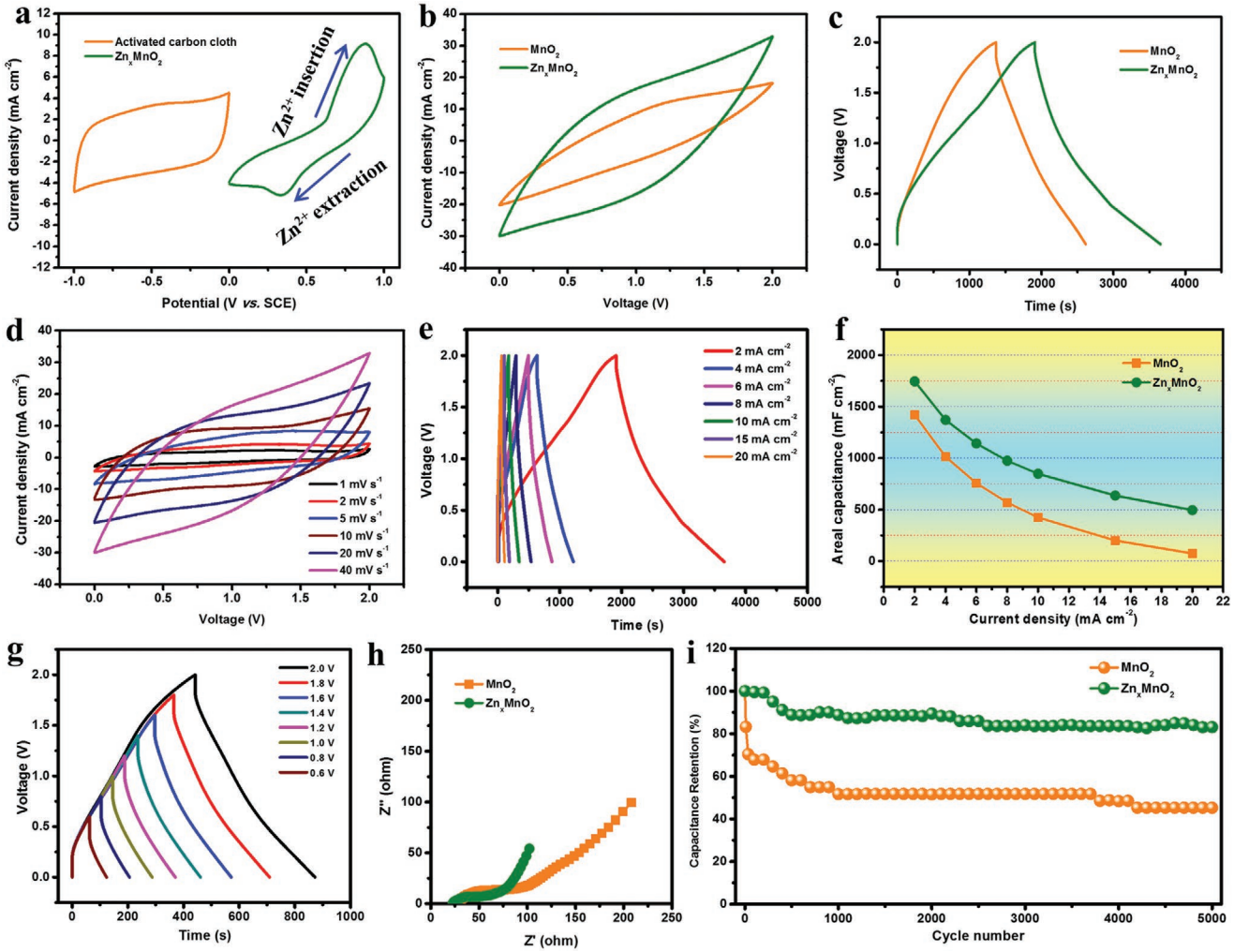

Figure 3. Electrochemical behavior of Zn-HSCs. a) CV curves of the ACC anode and the Zn_xMnO_2 cathode at a scan rate of 2 mV s^{-1}. b) Comparison of CV curves (40 mV) and c) GCD curves for the MnO_2//ACC and Zn_xMnO_2//ACC HSCs at 2 mA cm^{-2}. d) CV curves and e) GCD curves collected at different scan rates and current density of the Zn_xMnO_2//ACC Zn-HSCs. f) Areal capacitance as a function of the current density of the MnO_2//ACC and the Zn_xMnO_2//ACC Zn-HSCs. g) GCD curves of the Zn_xMnO_2//ACC HSCs collected at different potential windows at a fixed current density of 6 mA cm^{-2}. h) Nyquist plots and i) cycling performance of the MnO_2//ACC and Zn_xMnO_2//ACC Zn-HSCs at 15 mA cm^{-2}.

Zn_xMnO_2//ACC Zn-HSCs, which can faultlessly fulfill the avid demanding for wearable and high-performance energy storages.

To investigate the evolution of the crystal structure of the Zn_xMnO_2 cathode and ACC anode during the Zn-HSCs charge and discharge periods, the GCD curves are depicted in **Figure 5**a while the ex situ XRD patterns of Zn_xMnO_2 cathode are exhibited in Figure 5b. As we can see, the seven main characteristic peaks of typical α-MnO_2 are clearly depicted and the XRD patterns scarcely change during the charge and discharge processes, which indicates the tunnel-type crystal structure of the Zn_xMnO_2 nanowires is fully reversible and stable during the Zn-ion insertion/extraction processes and able to support the good cycling stability of Zn-HSCs. To further elucidate the reaction mechanism of the Zn_xMnO_2 nanowires, inductively coupled plasma (ICP) was conducted to six different states during the charge/discharge processes (Figure 5d). The original sample has a Zn/Mn molar ratio of 0.029. As expected, the Zn/Mn ratio increases with discharge and decreases with charge. In addition, the overall Zn/Mn ratio increase with cycling, and it reaches 0.596 after the third discharge process. The ICP results demonstrate that the Zn_xMnO_2 is able to trap Zn^{2+} in its tunnel structure, which may play a positive role in stabilizing the material. Moreover, the XPS spectra in Figure S18 (Supporting Information) verify the result of ICP. The intensity of peaks in Zn 2p spectra (Figure S18b, Supporting Information) prove that the Zn-ion truly insert into the sample after discharge to 0 V. To sum up, Figure 5e depicts the schematic illustration during insertion/extraction processes which reveals the zinc-storage mechanism in the Zn_xMnO_2 cathode.

Conversely, the XRD patterns (Figure 5c) of ACC changed with the adsorption/desorption processes. With the voltage increasing, there are four characteristic peaks at 11.3°, 32.8°, 34.9°, and 58.4° besides the peaks of the CC, corresponding to the $Zn_4SO_4(OH)6\cdot0.5(H_2O)$ and $ZnSO3\cdot2.5(H_2O)$. Clearly, it can be seen in the SEM images of different states (Figure 5f).

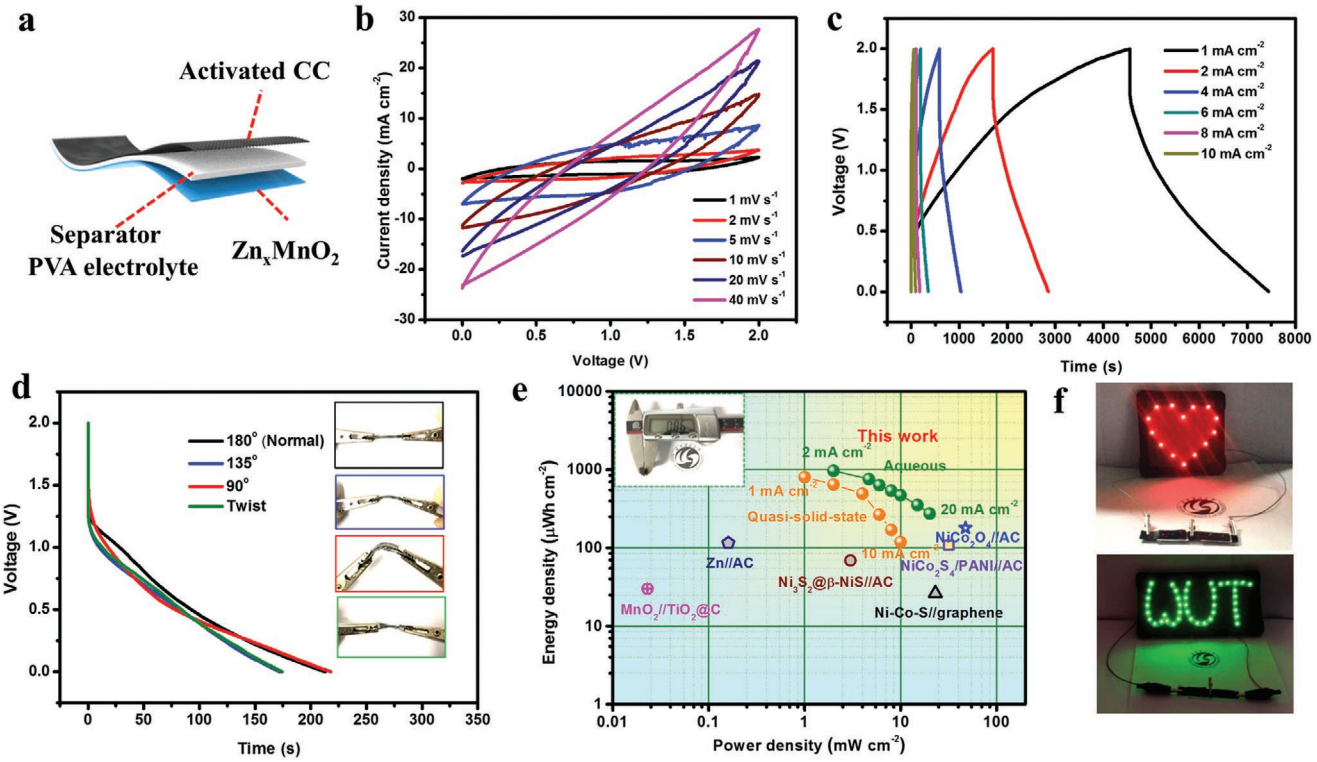

Figure 4. a) Schematic illustration of flexible quasi-solid-state Zn_xMnO_2//ACC Zn-HSCs. b) CV curves and c) GCD curves of the device. d) GCD curves under different bending conditions. e) Ragone plots of the quasi-solid-state Zn_xMnO_2//ACC Zn-HSCs. f) Photographs of LED lights powered by the quasi-solid-state Zn_xMnO_2//ACC devices in series.

From the state II to state IV (0.4–1.2 V), there only exist simplex desorption reaction in the ACC anode, and nothing grow on the surface through the SEM images. However, the SEM images exhibit that there are some nanosheets on the surface of the ACC anode from state V to state IX, it is believed that the phenomena are ascribed to the change of voltage. Besides the consistent adsorption/desorption reaction in the ACC anode, the Zn ions will be attracted to the surface of ACC anode in the range of high-voltage area during the charge/discharge processes, which can be confirmed by the XRD pattern that the $Zn_4SO_4(OH)6\cdot0.5(H_2O)$ and $ZnSO3\cdot2.5(H_2O)$ only exist during the range of high-voltage area. Partly, this process is considered to provide a certain amount of capacity for the Zn-HSCs. When discharged to 0 V, the SEM images (state X to state XI) return to the initial condition. Digital photo (Figure S19b, Supporting Information) of the Zn_xMnO_2 nanowire cathode and ACC anode at different states during the GCD (Figure S19a, Supporting Information) also proves the above results from a macro perspective.

The new configuration of the Zn-HSCs is schematically illustrated in **Figure 6**, consisting of the reactions during the charge/discharge processes. In the typical charge process, driven by applied voltage, the Zn-ion (Zn^{2+}) extractions happen in the Zn_xMnO_2 nanowires cathode while the SO_4^{2-} desorptions occur in the ACC anode. On the contrary, the Zn ions insert into the cathode and the SO_4^{2-} adsorb in the anode during the discharge process. Briefly, the reaction of the Zn-HSCs can be formulated as follows

$$\text{Cathode}: Zn_xMnO_2 - 2e^- \leftrightarrow Zn_yMnO_2 + Zn^{2+} \quad (1)$$

$$\text{Anode}: ACC + 5Zn^{2+} + 4OH^- + 2SO_4^{2-} + 4H_2O + 2e^- = ACC + Zn_4SO_4(OH)6\cdot0.5(H_2O) + ZnSO3\cdot2.5(H_2O) \quad (2)$$

The ionic and hydrated ionic radii of Zn are 0.75 and 4.04–4.30 Å, respectively.[34] α-MnO_2 has a 2 × 2 tunnel structure (4.6 × 4.6 Å), which can accommodate zinc ions in its tunnels. The δ-MnO_2 has a layered structure with interlayer spacing of ≈7 Å.[35] Theoretically, the layered structured δ-MnO_2 can store more zinc ions. However, the layered structure of δ-MnO_2 is prone to collapse in sulfate solution, leading to poor structural stability. The Zn^{2+} pre-intercalated tunnel structured α-MnO_2 (Zn_xMnO_2) has more stable characteristics during charge and discharge processes. The insertion/extraction of Zn-ion in tunnel structured Zn_xMnO_2 causes no structural transformation or collapse. The mechanism depicted in the figure of the Zn-HSCs is considered a sustainable way to achieve splendid cycling performance.

3. Conclusion

In summary, by pre-intercalation of Zn^{2+} in the hydrothermal process, we develop the tunnel-type Zn_xMnO_2 nanowires with ultrahigh mass loading of 12 mg cm^{-2} grown on mechanically flexible carbon cloth. When employed as the

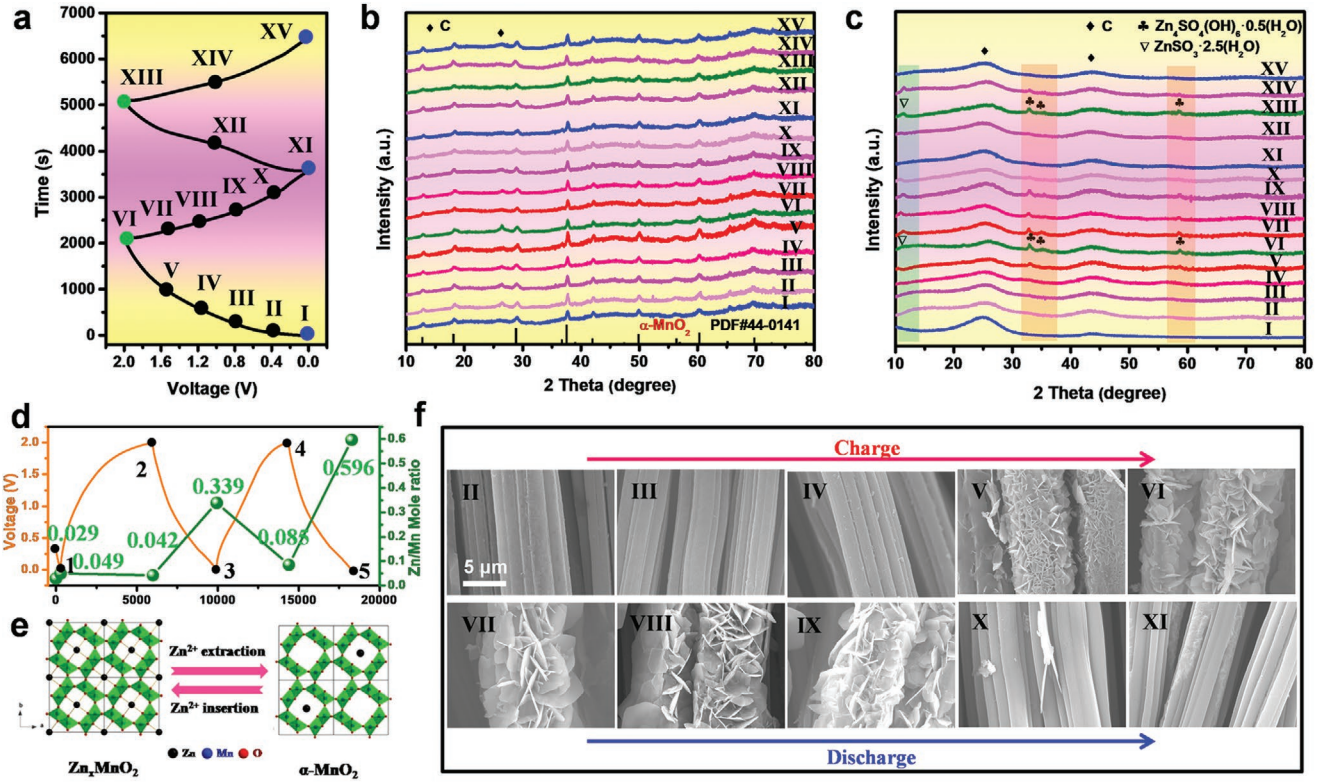

Figure 5. a) GCD curves of Zn_xMnO_2//ACC Zn-HSCs at 2 mA cm^{-2}. b,c) Corresponding the ex situ XRD patterns of Zn_xMnO_2 cathode and ACC anode at different charge/discharge states. d) The change of the Zn/Mn molar ratio during charging and discharging. e) Schematic illustration of the zinc-storage mechanism in the Zn_xMnO_2 electrode. f) SEM images of the ACC at charge/discharge states.

cathode in Zn-HSCs with either aqueous or quasi-solid-state electrolytes, they enable an ultrahigh areal capacitance of up to 1745.8 mF cm^{-2} at 2 mA cm^{-2}, a remarkable areal energy density of 969.9 μWh cm^{-2}, as well as long lifetime. By conducting systematic investigations into the growth, structures and charge/discharge process in the tunnel structured Zn_xMnO_2 nanowires, including ex situ, we have established key governing principles involved in the Zn-ion pre-intercalation, which leads to stable tunnel-type structure and outstanding electrochemical performance. The set of key performance parameters are comparable favorably with those of Zn-ion batteries, making them truly battery-level energy storage devices. Together with the excellent mechanical flexibility, the battery-level Zn-HSCs are promising to be applied in the new generation energy storage, where the large battery-supercapacitor gap is bridged.

4. Experimental Section

Synthesis of Zn_xMnO_2 Nanowires and MnO_2 Nanosheets Cathode: In a typical synthesis, the carbon cloth (2 cm × 3 cm) was firstly cleaned with ethanol, deionized (DI) water in ultrasonic machine, and then dried at 70 °C oven. 1.264 g $KMnO_4$ and 2.379 g $Zn(NO_3)_2{\cdot}6H_2O$ were dissolved in 75 mL DI water, and 2 mL 98% H_2SO_4 was added into this solution. After stirring the solution for 15 min, the resultant precursor solution and the pretreated CC were transferred to a Teflon-lined stainless steel autoclave (100 mL). The sealed autoclave was heated and maintained at

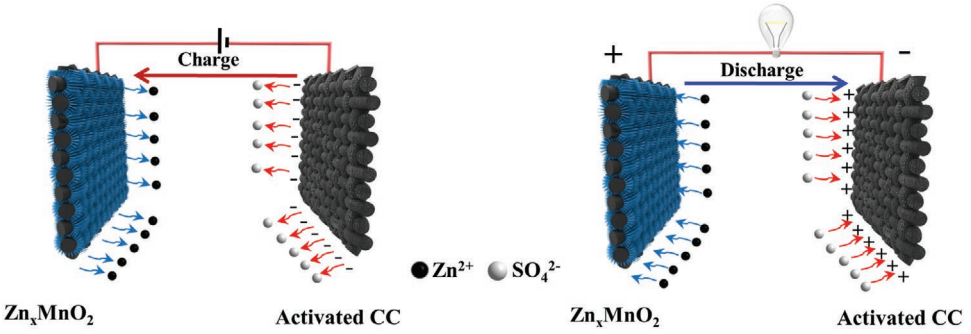

Figure 6. Schematic illustration of the designed aqueous Zn_xMnO_2//activated CC zinc-ion HSCs.

140 °C for 3.5 h. After cooling down to room temperature, the CC was cleaned with DI water and finally dried at 70 °C oven. The mass loading of the active material (Zn_xMnO_2) is measured to be 12.0 mg cm^{-2}, and the mass loading of CC is 11.3 mg cm^{-2}. The thickness of the whole electrode (Zn_xMnO_2 on CC) is around 0.42 mm. The MnO_2 nanosheets were prepared by a method similar to that of Zn_xMnO_2; however, no $Zn(NO_3)_2{\cdot}6H_2O$ was introduced during the synthesis. The mass loading of MnO_2 is measured to be 18.5 mg cm^{-2}, and the thickness of the whole electrode (MnO_2 on CC) is around 0.6 mm.

Synthesis of ACC Anode: The ACC anode was prepared through one-step thermal treatment of CC (2 cm × 3 cm) in air at 350 °C for 6 h.

Fabrication of Zn_xMnO_2//ACC Zinc-Ion Aqueous and Quasi-Solid-State HSCs: To fabricate the aqueous HSCs, where Zn_xMnO_2 nanowires (0.5 cm × 1.0 cm) acted as cathode electrode and ACC (0.5 cm × 1.0 cm) acted as anode electrode. 2 M $ZnSO_4$ and 0.4 M $MnSO_4$ were prepared as the electrolyte. Similarly, when assembling quasi-solid-state HSCs, the electrodes were invariable while PVA/$ZnCl_2$-$MnSO_4$ gel was employed as electrolyte with a NKK separator (Nippon Kodoshi Corporation). The gel electrolyte was prepared by mixing 2.0 g PVA, 5.45 g $ZnCl_2$, and 1.2 g $MnSO_4$ in 20 mL DI water, and then heated at 85 °C for 2 h with vigorous stirring. The thickness and volume of the fabricated quasi-solid-state Zn-HSCs devices are about 0.86 mm and 0.043 cm^3, respectively.

Materials Characterizations: XRD (Bruker D2) was employed to characterize the crystalline structures. The morphology and microstructure of the as-prepared materials were demonstrated by a field-emission SEM (JEOL-7100F) and TEM, HRTEM, high-angle annular dark-field scanning transmission electron microscopy (HAADF-STEM), EDS (Titan G2 60-300). Raman spectrum tests were characterized by Renishaw RM-1000 laser Raman microscopy system. The valence states of elements were detected by an XPS (ESCALAB 250Xi). The molar ratio of Zn and Mn elements of the Zn_xMnO_2 were measured by ICP optical emission spectrometer (Optima 4300DV).

Electrochemical Measurements: Electrochemical measurements data were performed with a CHI 760D electrochemical workstation. The electrochemical performance of the aqueous and quasi-solid-state Zn_xMnO_2//ACC Zn-HSCs was performed in a two-electrode system in the aqueous solution and gel, respectively.

Supporting Information

Supporting Information is available from the Wiley Online Library or from the author.

Acknowledgements

Q.C. and J.J. contributed equally to this work. The authors acknowledge the financial support from National Natural Science Foundation of China (21673171). J.W. acknowledges the support of the Ministry of Education (Tier 1, MOE, Singapore, R284-000-193-114) for research conducted in the National University of Singapore. Q.C. thanks Kwadwo Asare Owusu providing the anode material (activated carbon cloth) and support from the China Scholarship Council (CSC).

Conflict of Interest

The authors declare no conflict of interest.

Keywords

mechanical flexibility, pre-intercalation, ultrahigh areal energy density, zinc-ion hybrid supercapacitors, Zn_xMnO_2 nanowires

Received: January 6, 2020
Revised: February 10, 2020
Published online:

[1] a) B. Dunn, H. Kamath, J. M. Tarascon, *Science* **2011**, *334*, 928; b) P. Simon, Y. Gogotsi, *Nat. Mater.* **2008**, *7*, 845; c) J. B. Goodenough, *Energy Environ. Sci.* **2014**, *7*, 14.
[2] a) Y. Zhu, S. Murali, M. D. Stoller, K. J. Ganesh, W. Cai, P. J. Ferreira, A. Pirkle, R. M. Wallace, K. A. Cychosz, M. Thommes, D. Su, E. A. Stach, R. S. Ruoff, *Science* **2011**, *332*, 1537; b) L. L. Zhang, X. S. Zhao, *Chem. Soc. Rev.* **2009**, *38*, 2520; c) H. Jiang, P. S. Lee, C. Li, *Energy Environ. Sci.* **2013**, *6*, 41; d) J. Huang, B. G. Sumpter, V. Meunier, *Angew. Chem., Int. Ed.* **2008**, *47*, 520; e) S. Zhai, H. E. Karahan, C. Wang, Z. Pei, L. Wei, Y. Chen, *Adv. Mater.* **2019**, 1902387; f) M. Yu, Z. Wang, H. Zhang, P. Zhang, T. Zhang, X. Lu, X. Feng, *Nano Energy* **2019**, *65*, 103987; g) M. H. Yu, X. L. Feng, *Joule* **2019**, *3*, 338.
[3] a) J. W. Choi, D. Aurbach, *Nat. Rev. Mater.* **2016**, *1*, 16013; b) J. Jiang, Y. Li, J. Liu, X. Huang, C. Yuan, X. W. Lou, *Adv. Mater.* **2012**, *24*, 5166.
[4] a) B. Kang, G. Ceder, *Nature* **2009**, *458*, 190; b) M. R. Lukatskaya, B. Dunn, Y. Gogotsi, *Nat. Commun.* **2016**, *7*, 12467; c) P. Zhang, Y. Li, G. Wang, F. Wang, S. Yang, F. Zhu, X. Zhuang, O. G. Schmidt, X. Feng, *Adv. Mater.* **2019**, *31*, 1806005; d) G. Sun, H. Yang, G. Zhang, J. Gao, X. Jin, Y. Zhao, L. Jiang, L. Qu, *Energy Environ. Sci.* **2018**, *11*, 3367.
[5] a) F. Bonaccorso, L. Colombo, G. Yu, M. Stoller, V. Tozzini, A. C. Ferrari, R. S. Ruoff, V. Pellegrini, *Science* **2015**, *347*, 1246501; b) F. Zhang, T. Zhang, X. Yang, L. Zhang, K. Leng, Y. Huang, Y. Chen, *Energy Environ. Sci.* **2013**, *6*, 1623.
[6] D. P. Dubal, O. Ayyad, V. Ruiz, P. Gomez-Romero, *Chem. Soc. Rev.* **2015**, *44*, 1777.
[7] a) L. Shen, L. Yu, X.-Y. Yu, X. Zhang, X. W. Lou, *Angew. Chem., Int. Ed.* **2015**, *54*, 1868; b) Y. Ma, H. Chang, M. Zhang, Y. Chen, *Adv. Mater.* **2015**, *27*, 5296.
[8] a) H. Wang, C. Zhu, D. Chao, Q. Yan, H. J. Fan, *Adv. Mater.* **2017**, *29*, 1702093; b) J. Cui, S. Yao, Z. Lu, J. Q. Huang, W. G. Chong, F. Ciucci, J. K. Kim, *Adv. Energy Mater.* **2018**, *8*, 1704488.
[9] L. Fan, K. R. Lin, J. Wang, R. F. Ma, B. G. Lu, *Adv. Mater.* **2018**, *30*, 1800804.
[10] H. Wang, M. Wang, Y. Tang, *Energy Storage Mater.* **2018**, *13*, 1.
[11] M. Wang, C. Jiang, S. Zhang, X. Song, Y. Tang, H.-M. Cheng, *Nat. Chem.* **2018**, *10*, 667.
[12] M. C. Lin, M. Gong, B. Lu, Y. Wu, D.-Y. Wang, M. Guan, M. Angell, C. Chen, J. Yang, B. J. Hwang, H. Dai, *Nature* **2015**, *520*, 325.
[13] Y. Li, M. Gong, Y. Liang, J. Feng, J.-E. Kim, H. Wang, G. Hong, B. Zhang, H. Dai, *Nat. Commun.* **2013**, *4*, 1805.
[14] X. Zhang, Z. Pei, C. Wang, Z. Yuan, L. Wei, Y. Pan, A. Mahmood, Q. Shao, Y. Chen, *Small* **2019**, *15*, 1903817.
[15] L. Dong, X. Ma, Y. Li, L. Zhao, W. Liu, J. Cheng, C. Xu, B. Li, Q.-H. Yang, F. Kang, *Energy Storage Mater.* **2018**, *13*, 96.
[16] X. Ma, J. Cheng, L. Dong, W. Liu, J. Mou, L. Zhao, J. Wang, D. Ren, J. Wu, C. Xu, F. Kang, *Energy Storage Mater.* **2018**, *20*, 335.
[17] a) X. Ma, J. Cheng, L. Dong, W. Liu, J. Mou, L. Zhao, J. Wang, D. Ren, J. Wu, C. Xu, F. Kang, *Energy Storage Mater.* **2019**, *20*, 335; b) W. Sun, F. Wang, S. Hou, C. Yang, X. Fan, Z. Ma, T. Gao, F. Han, R. Hu, M. Zhu, C. Wang, *J. Am. Chem. Soc.* **2017**, *139*, 9775.
[18] G. Liu, H. Huang, R. Bi, X. Xiao, T. Ma, L. Zhang, *J. Mater. Chem. A* **2019**, *7*, 20806.
[19] B. Wu, G. Zhang, M. Yan, T. Xiong, P. He, L. He, X. Xu, L. Mai, *Small* **2018**, *14*, 1703850.
[20] K. Natarajan, M. Saraf, S. M. Mobin, *Nanoscale* **2018**, *10*, 13250.
[21] Y. Xie, Y. Yu, X. Gong, Y. Guo, Y. Guo, Y. Wang, G. Lu, *CrystEngComm* **2015**, *17*, 3005.
[22] a) T. Zhai, X. Lu, Y. Ling, M. Yu, G. Wang, T. Liu, C. Liang, Y. Tong, Y. Li, *Adv. Mater.* **2014**, *26*, 5869; b) X. F. Lu, L. F. Gu, J. W. Wang, J. X. Wu, P. Q. Liao, G. R. Li, *Adv. Mater.* **2017**, *29*, 1604437; c) M. Yu, Y. Han, X. Cheng, L. Hu, Y. Zeng, M. Chen, F. Cheng, X. Lu, Y. Tong, *Adv. Mater.* **2015**, *27*, 3085.
[23] a) J. Han, K. Wang, W. Liu, C. Li, X. Sun, X. Zhang, Y. An, S. Yi, Y. Ma, *Nanoscale* **2018**, *10*, 13083; b) S. Wang, Y. Shao, W. Liu,

Y. Wu, X. Hao, *J. Mater. Chem. A* **2018**, *6*, 13215; c) M. Hu, C. Cui, C. Shi, Z. S. Wu, J. Yang, R. Cheng, T. Guang, H. Wang, H. Lu, X. Wang, *ACS Nano* **2019**, *13*, 6899; d) K. Jayaramulu, D. P. Dubal, B. Nagar, V. Ranc, O. Tomanec, M. Petr, K. K. R. Datta, R. Zboril, P. Gomez-Romero, R. A. Fischer, *Adv. Mater.* **2018**, *30*, 1705789; e) B. T. Liu, X. M. Shi, X. Y. Lang, L. Gu, Z. Wen, M. Zhao, Q. Jiang, *Nat. Commun.* **2018**, *9*, 1375; f) I. W. Ock, J. W. Choi, H. M. Jeong, J. K. Kang, *Adv. Energy Mater.* **2018**, *8*, 1702895.

[24] a) P. Zhang, Y. Li, G. Wang, F. Wang, S. Yang, F. Zhu, X. Zhuang, O. G. Schmidt, X. Feng, *Adv. Mater.* **2019**, *31*, 1806005; b) L. Dong, X. Ma, Y. Li, L. Zhao, W. Liu, J. Cheng, C. Xu, B. Li, Q.-H. Yang, F. Kang, *Energy Storage Mater.* **2018**, *13*, 96.

[25] J. G. Wang, Z. Zhang, X. Zhang, X. Yin, X. Li, X. Liu, F. Kang, B. Wei, *Nano Energy* **2017**, *39*, 647.

[26] W. Zuo, C. Xie, P. Xu, Y. Li, J. Liu, *Adv. Mater.* **2017**, *29*, 1703463.

[27] a) W. Liu, M.-S. Song, B. Kong, Y. Cui, *Adv. Mater.* **2017**, *29*, 1603436; b) Y. Yang, Q. Huang, L. Niu, D. Wang, C. Yan, Y. She, Z. Zheng, *Adv. Mater.* **2017**, *29*, 1606679.

[28] M. Yan, P. He, Y. Chen, S. Wang, Q. Wei, K. Zhao, X. Xu, Q. An, Y. Shuang, Y. Shao, K. T. Mueller, L. Mai, J. Liu, J. Yang, *Adv. Mater.* **2018**, *30*, 1703725.

[29] F. Wan, L. Zhang, X. Dai, X. Wang, Z. Niu, J. Chen, *Nat. Commun.* **2018**, *9*, 1656.

[30] N. Zhang, F. Cheng, Y. Liu, Q. Zhao, K. Lei, C. Chen, X. Liu, J. Chen, *J. Am. Chem. Soc.* **2016**, *138*, 12894.

[31] K. Lu, B. Song, Y. Zhang, H. Ma, J. Zhang, *J. Mater. Chem. A* **2017**, *5*, 23628.

[32] B. Sambandam, V. Soundharrajan, S. Kim, M. H. Alfaruqi, J. Jo, S. Kim, V. Mathew, Y.-K. Sun, J. Kim, *J. Mater. Chem. A* **2018**, *6*, 3850.

[33] a) L. Yao, Q. Wu, P. Zhang, J. Zhang, D. Wang, Y. Li, X. Ren, H. Mi, L. Deng, Z. Zheng, *Adv. Mater.* **2018**, *30*, 1706054; b) Y. Zeng, X. Zhang, Y. Meng, M. Yu, J. Yi, Y. Wu, X. Lu, Y. Tong, *Adv. Mater.* **2017**, *29*, 1700274.

[34] D. Chao, H. J. Fan, *Chem* **2019**, *5*, 1359.

[35] P. He, Q. Chen, M. Yan, X. Xu, L. Zhou, L. Mai, C. W. Nan, *EnergyChem* **2019**, *1*, 100022.